

Wireless multichannel optogenetic stimulators enabled by narrow bandwidth resonant tank circuits



Ammar Aldaoud^{a,*}, Artemio Soto-Breceda^{b,f,g}, Wei Tong^{a,b,c}, Greg Conductier^d, Mary A. Tonta^d, Harold A. Coleman^d, Helena C. Parkington^d, Iain Clarke^d, Jean-Michel Redoute^e, David J. Garrett^a, Steven Prawer^a

^a School of Physics, University of Melbourne, Parkville, Victoria, Australia

^b National Vision Research Institute, Australian College of Optometry, Carlton, Victoria, Australia

^c Department of Optometry and Vision Sciences, University of Melbourne, Parkville, Victoria, Australia

^d Department of Physiology and Biomedicine Discovery Institute, Monash University, Clayton, Victoria, Australia

^e Electrical and Computer Systems Engineering, Monash University, Clayton, Victoria, Australia

^f Department of Biomedical Engineering, University of Melbourne, Parkville, Victoria, Australia

^g Data 61, CSIRO, Docklands, Victoria, Australia

ARTICLE INFO

Article history:

Received 31 May 2017

Received in revised form 1 December 2017

Accepted 21 December 2017

Available online 26 December 2017

Keywords:

Optogenetics

Wireless power

Inductive

Multichannel

In-vitro

Retinal ganglion cells

Human embryonic kidney cells

Channelrhodopsin

ABSTRACT

Optogenetic neuromodulation is a powerful technique used to study cells that form part of neuronal circuits. Light stimulation of neurons has led to a deeper understanding of autism, schizophrenia and depression. However, researchers are often limited to tethered systems involving percutaneous plugs, hence, wireless power transmission to an implantable device is desirable. This work details the design, fabrication and testing of multichannel wirelessly powered optogenetic devices. By employing several carefully tuned resonant tank circuits, this work demonstrates the ability to address a scalable number of light sources on a single device. Single channel, dual channel and 16 channel devices were fabricated, achieving light output readings of up to 15mW at 473nm, suitable for activating channelrhodopsin. Wireless power transmission was characterized in air and porcine tissue for implant depths up to 30mm, making device implantation feasible. The device was successful in activating endogenous (in retinal ganglion cells) and exogenously transfected channelrhodopsin in human embryonic kidney cells, providing biological validation. The significance of this approach is the removal of power-hungry and area-consuming electronics from the implant, while the ability to address and modulate individual light sources is maintained by shifting this complexity to the external wireless power transmitter.

© 2017 Elsevier B.V. All rights reserved.

1. Introduction

Optogenetics is an emergent field that has been developing rapidly for the past ten years. The ability to control cells precisely using light has permitted researchers to interrogate what were previously mysterious neuronal circuits. Advancements have included a deeper understanding of the neurological bases for sleep [1], depression [2] and Parkinson's disease [3]. For the most part, channelrhodopsin-2 (ChR2) and halorhodopsin (NphR) proteins sensitive to blue and yellow light respectively, have been popular as they allow cells to be activated or silenced with high spatiotemporal

resolution [4]. Thus, techniques for delivering these wavelengths of light to cells are desirable.

Most light delivery techniques rely on tethered systems, which permit the delivery of significant optical power. This can involve either a percutaneous fiber optic cable [5] or a wired micro-LED [6]. It is desirable to demonstrate devices of implantable size that can be wirelessly powered as they are a step closer towards using optogenetic strategies to manage disease in humans. Montgomery et al. [7] have demonstrated a single-channel wirelessly powered implant, to activate ChR2 expressed in a mouse model and Park et al. [8] extend the concept [7] by creating an addressable dual channel implant, also verified in a mouse model. Both approaches use microwave frequency signals, above 1GHz, to power their devices. Shin et al. [9] report a 10mm diameter flexible and fully implantable device that is powered at 13.56 MHz, reducing the transmission frequency, which can be desirable, as higher frequencies are more

E-mail addresses: ammar.ald.91@gmail.com, aaldaoud@student.unimelb.edu.au (A. Aldaoud).

* Corresponding author.

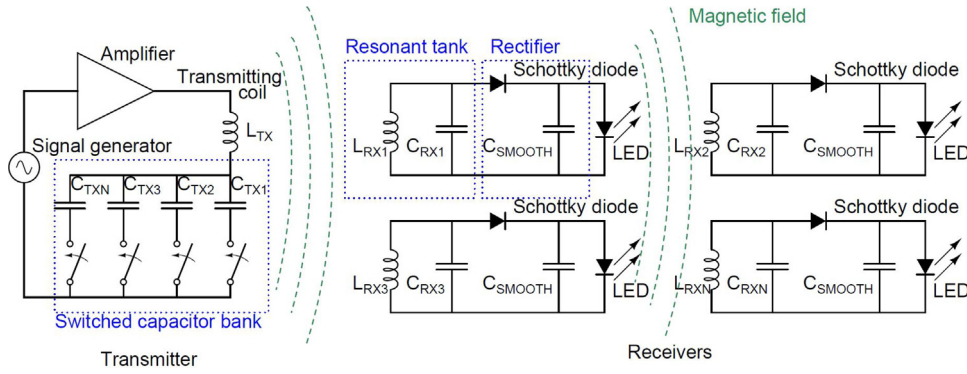


Fig. 1. Multi-resonant coil electronic schematic. The transmitter is tuned to the same resonant frequency as one of the receiving devices.

likely to cause tissue heating [10]. This work extends previous approaches [9] by demonstrating that several coils can be tuned to receive at different frequencies to fabricate a device with several channels. Several electronic designs have been proposed to address the need for wirelessly powered optogenetic stimulators. An example is where an inductive power link to an integrated circuit drives an array of light sources [11]. Although such designs are powerful, they are typically unavailable to the research community due to the requirement of a custom integrated circuit. Most other demonstrations involve a wirelessly powered head borne device on a mouse [12–14].

Optogenetic light sources need to meet several design requirements to be effective. Light intensity needs to be sufficient to activate cells, the light source needs to be modulated and ideally, several addressable light channels need to be made available [15]. This work describes a novel wireless power technique to meet these needs that removes power-hungry and area-consuming electronics from the implantable device. Furthermore, readily available components are used. The need for varying intensity is met by changing the amplitude of the wireless power signal. By modulating the transmitted signal, the light source is modulated in turn. Individual light sources are addressed by tuning each receiving channel to a different frequency, meaning the transmitter activates a light source by varying its carrier frequency. The design equations, fabrication, measurement results and in-vitro cell studies are detailed in this work.

2. Materials and methods

2.1. Design principal and equations

Fig. 1 depicts an overview of the wireless n -channel optogenetic system and Eqs. (1) and (9) outline the design parameters. On the transmitter side a signal generator feeds an amplifier that drives a series-resonant LC tank circuit formed by L_{TX} and C_{TX1} , C_{TX2} to C_{TXN} . Jegadeesan & Yong-Xin identify that the series resonant topology on the transmitter side improves power transfer efficiency and that a parallel resonant tank on the receiving side is suitable for lower frequencies and larger loads, which is the case herein [16]. Hence, each receiving device contains a parallel resonant tank circuit formed by L_{RXN} and C_{RXN} . The parallel tank serves two purposes: to receive power at a given transmission frequency and to act as a band pass filter to stop other frequencies powering up the device. The Schottky diode rectifies the incoming AC signal and C_{SMOOTH} removes the carrier frequency, while maintaining any frequency modulation present in the signal. This in turn drives the LED on the output.

To transmit and receive power efficiently L_{RX1} must have high quality factor, denoted Q_L . This is calculated using Eq. (1), where L

is the inductance of the coil and R_L is the parasitic series resistance of the inductor at a given frequency.

$$Q_L = \frac{2\pi fL}{R_L} \quad (1)$$

A desired resonant frequency is chosen, denoted as f_{RES} in Eq. (2), which permits calculation of the matching capacitor C_{RX1} .

$$f_{RES} = \frac{1}{2\pi\sqrt{L_{RXN}C_{RXN}}} \quad (2)$$

Q_{PAR} denotes the parallel resonant quality factor of the tank circuit and is different to Q_L . A high Q_L is required to ensure effective wireless power reception, whereas a high Q_{PAR} is required for narrow frequency selectivity. V_{LED} and I_{LED} denote the voltage and current operating point of the LED used.

$$Q_{PAR} = \frac{V_{LED}}{I_{LED}} \sqrt{\frac{C_{RXN}}{L_{RXN}}} \quad (3)$$

L_{RX1} receives maximum power at f_{RES} and half the amount of power at f_{LOW} and f_{HIGH} , which are calculated using Eqs. (4) and (5). The other devices are then tuned such that their resonant frequency is spaced apart from f_{LOW} and f_{HIGH} meaning they cannot be activated when the transmitter is tuned to f_{RES} for L_{RX1} . This design procedure is then repeated for n devices up to L_{RXN} .

$$f_{LOW} = f_{RES} - \frac{f_{RES}}{2Q_{PAR}} \quad (4)$$

$$f_{HIGH} = f_{RES} + \frac{f_{RES}}{2Q_{PAR}} \quad (5)$$

C_{SMOOTH} is a less critical value and is chosen such that f_{RES} is filtered out, while any modulation in the transmitted signal, denoted by f_{MOD} is maintained. Hence, C_{SMOOTH} must fall into the bounds shown in equation 6.

$$f_{MOD} < \frac{I_{LED}}{2\pi V_{LED} C_{SMOOTH}} < f_{RES} \quad (6)$$

Once the number of devices condition is satisfied, L_{TX} and several capacitor values denoted by C_{TX1} , C_{TX2} ... C_{TXN} are chosen such that the transmitter can match the resonant frequency of any receiving device. The circuit simulation software SPICE can then be used to verify channel spacing, power output and LED modulation.

$$f_{RES} = \frac{1}{2\pi\sqrt{L_{TX}C_{TXN}}} \quad (7)$$

2.2. Fabrication and testing process

Single channel, dual channel and 16 channel devices were fabricated for testing. Each receiving coil was wound around a 2 mm

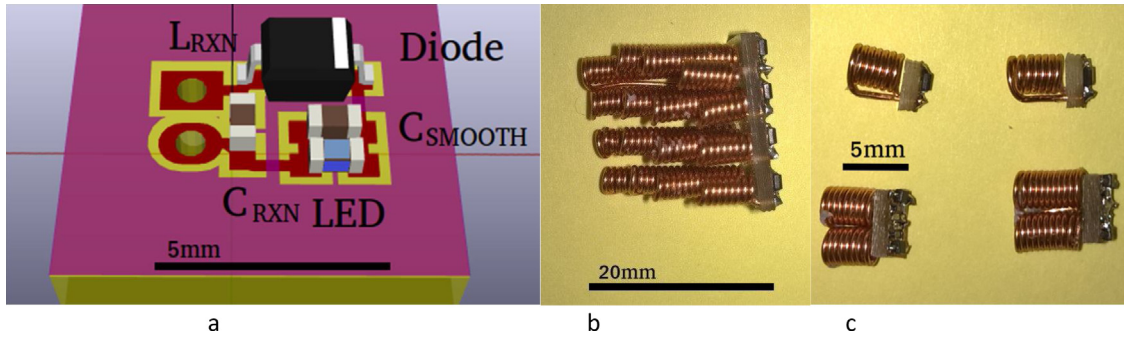


Fig. 2. a) 3D rendering of component layout for a single channel receiver b) Side-view of 16 channel device showing inductive coils c) Single channel and dual channel devices.

coil former with 0.5 mm diameter enameled copper wire. Each printed circuit board was milled using T-tech tools Quick Circuit Prototyping Systems. Single channel, dual channel and 16 channel boards measured 5 mm by 2.5 mm, 5 mm by 5 mm and 11 mm by 18 mm respectively. L_{RXN} varies between 8 and 20 turns and the corresponding inductance was approximated using Eq. (8) [17].

$$L \approx N^2 \mu_0 \left(\frac{D}{2} \right) \left(\ln \left(\frac{8D}{d} \right) - 2 \right) \quad (8)$$

Where N is the number of turns, D is the loop diameter, d is the diameter of the wire and μ_0 is the permeability of free space. An alternate equation for the inductance of a solenoid is given by equation 9.

$$L \approx \frac{N^2 \mu_0 \pi D^2}{4h} \quad (9)$$

Where h is the height of the solenoid and the other quantities are as previously defined. C_{RXN} varies in value from 910 pF to 1200 pF and are 0402 sized (1mm by 0.5 mm) surface mount devices with NPO dielectric. L_{RXN} and C_{RXN} were chosen based on the design equations specified previously. The Schottky diodes used were MMDL301T1G fast switching silicon hot-carrier diodes, which are capable of forward currents of up to 100 mA while maintaining a low forward voltage drop. C_{SMOOTH} is a 0402 NPO 1nF capacitor and the LEDs chosen are also 0402 sized. 473 nm blue LEDs and 590 nm yellow LEDs were chosen, operating at $V_{LED} = 2.8$ V, $I_{LED} = 5$ mA and $V_{LED} = 2$ V, $I_{LED} = 20$ mA respectively. Fig. 2 depicts the component layout of a single channel on a printed circuit board, as well as two single channel, two dual channel and one 16 channel device.

The signal generator used was a Rigol DG4162, which fed an LZYZ-22+, 0.1–200 MHz amplifier with 43 dB gain from Mini-Circuits. The output power of the signal generator was measured using an RF power meter called a SynthNV from WindFreak Technologies, permitting the transmitter output power to be calculated. The transmitting coil was made by winding four turns of 1 mm diameter enameled copper wire around a 30 mm diameter coil former. This was connected in series with a switched capacitor bank of values 47 pF, 68 pF, 82 pF and 100 pF. Layers of 1.1 mm glass slides were used to separate the transmitting coil and the receiving device. The light output power of the LEDs was measured using a Field Max laser power meter from Coherent. Measurements were taken in a dark room and the LED was placed as close to the light output power sensor as possible. The transmitted carrier signal was square wave modulated at 2 Hz, 5 Hz, 10 Hz and 20 Hz. A photodiode was connected to an LM358 operational amplifier circuit and powered by a 5V supply. The photodiode was placed near the powered LED and a Lecroy 6100A oscilloscope was used to measure the voltage change on the output of the operational amplifier with respect to time. Post processing of the time domain signal from the oscilloscope was done in MATLAB. The test set up used is depicted in Fig. 3. Power output, modulation and channel selectivity were measured

and verified. All measurements were repeated with the volume between the transmitting coil and device replaced with porcine tissue, with the devices embedded in porcine tissue to simulate device implantation. The influence of angular displacement was also monitored.

2.3. Quality factor measurement process

Quality factor measurements were taken for each receiving coil, as well as each resonant circuit in each channel. To characterise each receiving inductor L_{RX} , separate identical coils were fabricated with 7, 8, 11, 12, 16 and 20 turns using a 2 mm coil former. The coils were connected in parallel to a 470 pF reference capacitor and an SMA connector. A signal generator was configured with a 50 Ω source impedance and used to drive the parallel resonant LC tank and the voltage across the LC tank was measured with an oscilloscope. High impedance AC coupling was used to avoid loading the resonator. Moreover, the oscilloscope input was bandwidth limited to avoid harmonic influence on the measurement. The quality factor of the capacitor is assumed to be orders of magnitude higher than the inductor. Hence, the quality factor of the parallel LC tank formed with the 470 pF reference capacitor was taken to be Q_L of Eq. (1). The signal generator frequency was varied until the maximum peak to peak voltage was seen on the oscilloscope, indicating resonance. Then, the inductance of the coil was calculated using Eq. (2). The upper and lower frequencies, f_H and f_L at which the maximum voltage became attenuated by 3dB were also recorded. The coil quality factor was then calculated using Eq. (10). The measurement process was repeated for all coils in air, as well as in porcine tissue.

$$Q = \frac{f_{RES}}{f_H - f_L} \quad (10)$$

Q_{PAR} was then measured using two different methods. Eq. (3) was used to calculate Q_{PAR} using the measured inductance L_{RX} . Measurement results for Q_{PAR} were also verified with the same process used to measure Q_L and Eq. (10).

2.4. Simulation process

Electromagnetic simulation software was used to determine how the wireless link heats tissue. A volume of muscle tissue measuring 100 mm by 100 mm by 50 mm was created in the simulation software CST Microwave Studio[®]. Four turns of 1 mm diameter wire with an inner diameter of 30 mm was placed 1 mm above the tissue volume. Simulations were run for frequencies between 5 MHz and 25 MHz in 5 MHz steps. The input power to the coil was increased at each frequency step until a specific absorption rate (SAR) threshold was reached. The SAR safety limit was taken as 1.6W/kg averaged over 1 g of tissue [18].

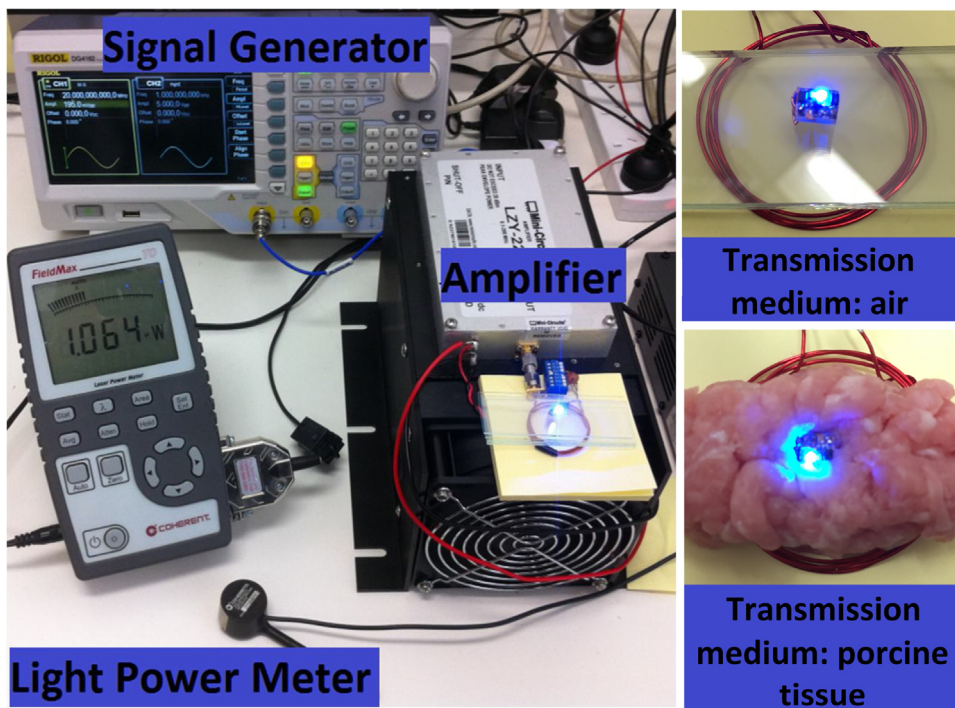


Fig. 3. a) Experimental setup used to test light output power, modulation and channel selectivity of optogenetic devices. Devices were tested in air and porcine tissue.

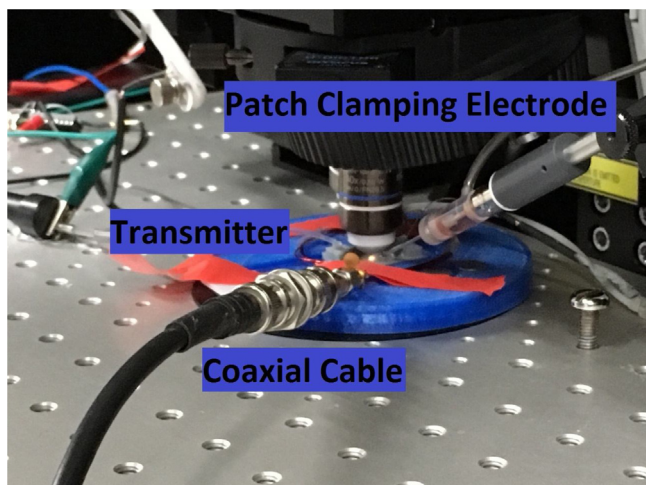


Fig. 4. Electrophysiological set up configuration used for in-vitro cell testing. The transmitting coil can be seen around the recording chamber whereas the receiving device is under the cover slip.

2.5. In-vitro cell testing

Whole cell recordings of a retinal ganglion cell (RGC) were performed using the current-clamp technique described previously [19–22], shown in Fig. 4. In brief, an adult rat was anaesthetized with a mixture of Ketamine (100 mg/kg) and Xylazine (10 mg/kg). After enucleation, the rat was killed with an intracardiac injection of Lethobarb (1ml). The retina was then dissected, flat-mounted with RGC side up on a glass coverslip, placed in a recording chamber and superfused (3–8 ml/min) with carbogenated Ames' medium at room temperature. A single channel device was mounted under the cover slip and the transmitting coil was mounted around the recording chamber prior to patch clamping. To obtain a whole cell recording a sharp glass pipette was used to make a hole in the inner limiting membrane to expose the RGC to be tested. The RGC was

then patch-clamped with a recording glass pipette filled with 6.5 μ L of 90% potassium gluconate, 5% energy cache, 2.5% biocytin and 2.5% Alexa Fluor (Thermo Fisher Scientific Inc.). The impedance of the recording pipette was 6 M Ω . Once a quality recording was established, the single channel device was modulated at 0.5 Hz, 1 Hz and 2 Hz. Following the recording, superfusion was stopped and 1.5 μ l of 10 mM sulforhodamine 101 was added to the recording chamber. The recorded RGC was imaged with a confocal microscope and the morphology was reconstructed with depth imaging. All animal experiments were conducted as per the policies of National Health and Medical Research Council of Australia and were approved by the Animal Ethics Committee of the University of Melbourne.

A dual channel device was tested using Human Embryonic Kidney cells. (HEK)-293 cells were grown on 9 mm glass coverslips in DMEM in the presence of 10% fetal calf serum, penicillin and streptomycin [4]. Cells were then transfected with pAAV-EF1a-hChr2(H134R)-EYFP using calcium chloride. Two days later, the cells were studied using patch-clamp electrophysiology with a dual channel device mounted under the cover slip. The transmitter was driven with a 13.4 MHz and 15.6 MHz carrier to drive the yellow and blue LEDs respectively and modulated at 1 Hz, 2 Hz, 5 Hz and 10 Hz for each colour. The cell response was recorded.

3. Results

3.1. Inductance and quality factor

Fig. 5 depicts the inductance and quality factor of each receiving coil. Eqs. (8) and (9) are both used to calculate the inductance of a solenoidal coil for comparison. Eqs. (8) and (9) overestimate and underestimate the measured inductance, respectively. The quality factor of each coil declines as the number of turns is increased. From Eq. (1), this means that extra turns are contributing more series resistance than inductive reactance to the total impedance of the coil. The coil characterization results did not differ in porcine tissue by more than 3%. Hence, the results are taken to be the same in air and porcine tissue.

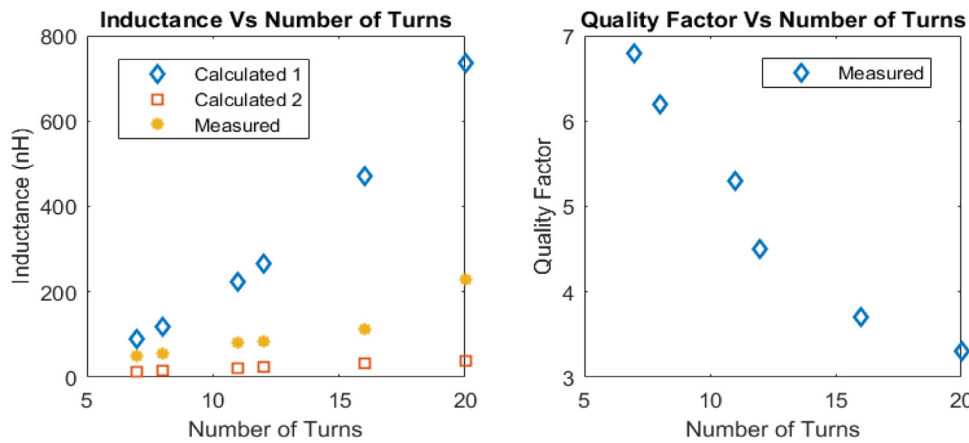


Fig. 5. Left) Measured and calculated inductance of receiving coils, L_{RX} . Coils are of diameter 2 mm with 7, 8, 11, 12, 16 and 20 turns. ‘Calculated 1’ and ‘Calculated 2’ are obtained using Eqs. (8) and (9) respectively. Right) Measured quality factor for each coil, denoted Q_L in Eq. (1). Not to be confused with Q_{PAR} in Eq. (3).

3.2. Device characterisation results

Tables 1–3 describe the parameters for each single channel, dual channel and 16 channel device. L_{RX} is calculated using equation eight and in turn, f_{RES} is calculated using equation two. The value of f_{RES} is also measured by finding the frequency for which maximum LED brightness is observed. Calculated and measured values for f_{RES} are compared in each table. Q_{PAR} is the quality factor of the resonant circuit loaded with the LED, indicating the selectivity of each channel. The P_{OUT} / P_{MAX} column of Table 3 was obtained by the following process. The 16 channel device was placed 5 mm away from the transmitter coil at an input power of 5 W. The maximum light output power from a single channel was recorded and

in this case, it was channel 11 at 4.38 mW and this value was taken to be P_{MAX} . All the other channel output powers were normalized with respect to P_{MAX} to provide a point of comparison. Measurements of L_{RX} , f_{RES} and Q_{PAR} were found to differ by no more than 3% when measured in porcine tissue as compared to air. Hence, the measurements listed are for both air and porcine tissue.

3.3. Light output power as a function of distance

The light output power of single channel device 2 is plotted against the transmission distance in Fig. 6. The transmitted signal is a sine wave of 20 MHz delivered with varying power as identified in the figure legend. A value of light output power in mW/mm^2

Table 1
Single Channel Device Parameters.

	Inductor #turns	L_{RX} Calculated (nH)	L_{RX} Measured (nH)	C_{RX} (pF)	f_{RES} Calculated (MHz)	f_{RES} Measured (MHz)	Q_{PAR}
Device 1	7	14 or 90	49	1200	15.3 or 38.8	19.0	15.6
Device 2	7	14 or 90	49	1000	16.8 or 42.5	20.0	14.3

Table 2
Dual Channel Device Parameters.

Device 1	Inductor #turns	L_{RX} Calculated (nH)	L_{RX} Measured (nH)	C_{RX} (pF)	f_{RES} Calculated (MHz)	f_{RES} Measured (MHz)	Q_{PAR}
Yellow (590 nm)	11	22 or 223	81	1200	9.7 or 31	13.4	12.2
Blue (473 nm)	11	22 or 223	81	910	11.2 or 35.6	15.6	10.6
Device 2							
Yellow (590 nm)	8	16 or 118	56	1200	13.4 or 36.3	16.2	14.6
Blue (473 nm)	8	16 or 118	56	910	15.4 or 41.7	17.8	12.7

Table 3
16 Channel Device Parameters.

Channel number	Coil #turns	L_{RX} Calculated (nH)	L_{RX} Measured (nH)	C_{RX} (pF)	f_{RES} Calculated (MHz)	f_{RES} Measured (MHz)	Q_{PAR}	P_{OUT} / P_{MAX}
1	20	40 or 737	230	1200	5.4 or 22.9	12.9	7.2	0.68
2	20	40 or 737	230	1100	5.6 or 24.0	13.6	6.9	0.79
3	20	40 or 737	230	1000	5.9 or 25.2	14.2	6.6	0.77
4	20	40 or 737	230	910	6.1 or 26.4	15.1	6.3	0.78
5	16	32 or 472	112	1200	6.7 or 25.7	14.7	10.4	0.92
6	16	32 or 472	112	1100	7.0 or 26.8	15.4	9.9	0.98
7	16	32 or 472	112	1000	7.3 or 28.1	16.0	9.4	0.97
8	16	32 or 472	112	910	7.7 or 29.5	17.1	9.0	0.98
9	12	24 or 265	85	1200	8.9 or 29.7	16.8	11.9	0.98
10	12	24 or 265	85	1100	9.3 or 31.0	18.8	11.4	1
11	12	24 or 265	85	1000	9.8 or 32.5	18.2	10.8	0.99
12	12	24 or 265	85	910	10.2 or 34.1	19.1	10.3	0.98
13	8	16 or 118	81	1200	13.4 or 36.3	22.8	12.2	0.69
14	8	16 or 118	81	1100	14.0 or 37.9	24	11.7	0.67
15	8	16 or 118	81	1000	14.7 or 39.8	25.5	11.1	0.65
16	8	16 or 118	81	910	15.4 or 41.7	26.4	10.6	0.61

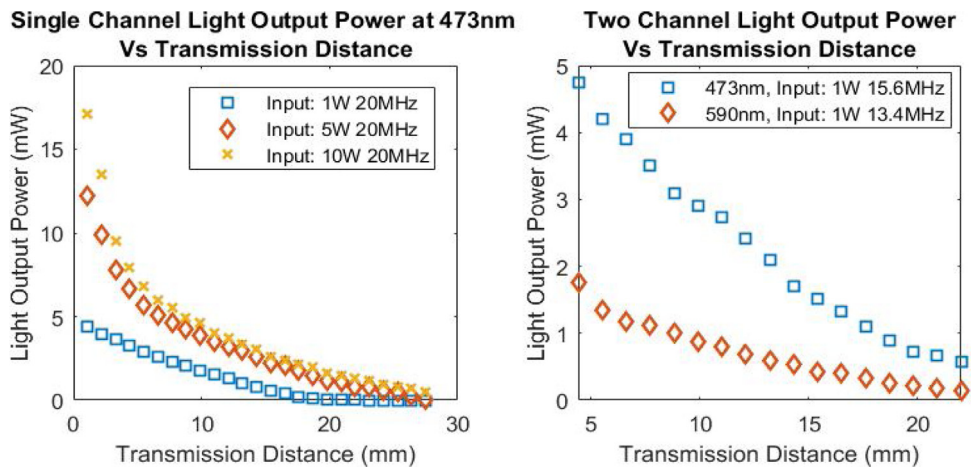


Fig. 6. Light output power plotted against wireless power transmission distance for a single channel and dual channel device.

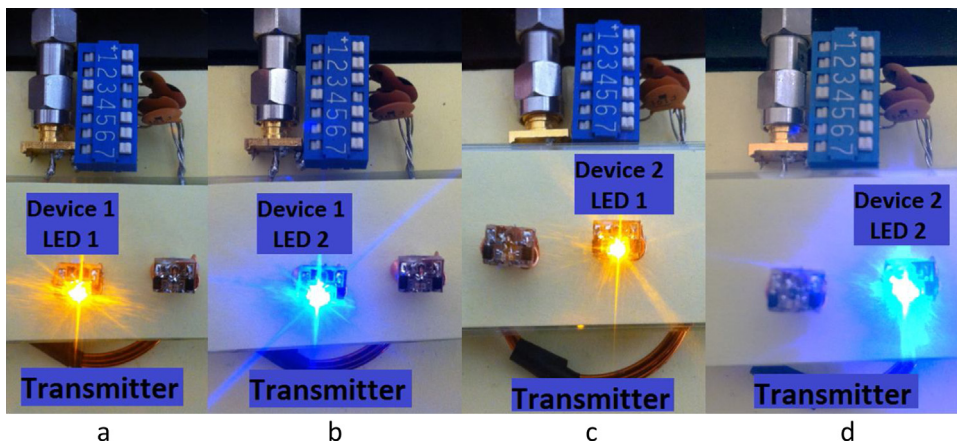


Fig. 7. Channel selectivity demonstrated across two, dual channel devices by varying transmission carrier frequency a) 13.4 MHz b) 15.6 MHz c) 16.2 MHz d) 17.8 MHz.

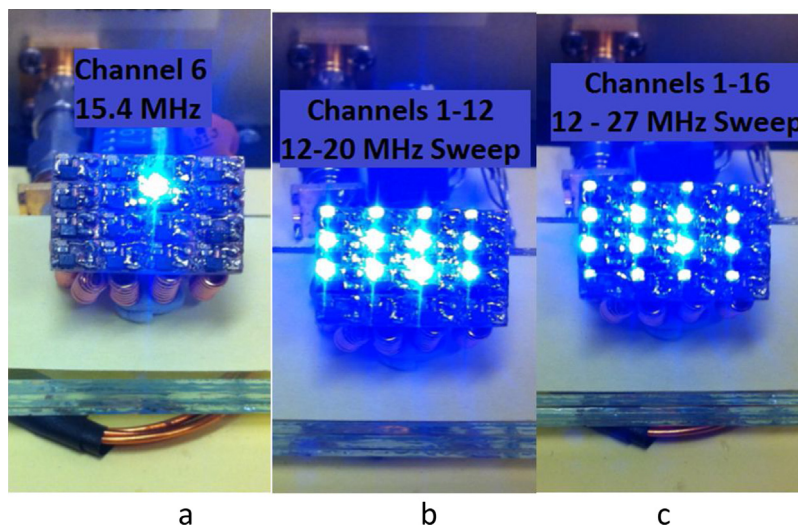


Fig. 8. 16 Channel device channel selectivity a) 15.4 MHz single channel selection b) frequency sweep from 12 MHz to 20 MHz selecting channels 1 to 12 c) frequency sweep from 12 MHz to 27 MHz selecting channels 1–16.

is often desirable as a point of comparison between various published works. This can be calculated by taking the surface area of the LED into consideration. Each LED is an 0402 surface mount device, which is 1 mm by 0.5 mm in surface area. Hence, a mW/mm² value can be obtained by dividing each measured output power by

0.5 mm². Results obtained in porcine tissue were close to identical to those obtained using glass slides to separate the device and transmitter coil, differing by no more than 3%.

The light output power of dual channel device 2 is shown in Fig. 6. Once again, the 13.4 MHz and 15.6 MHz signals are sine waves

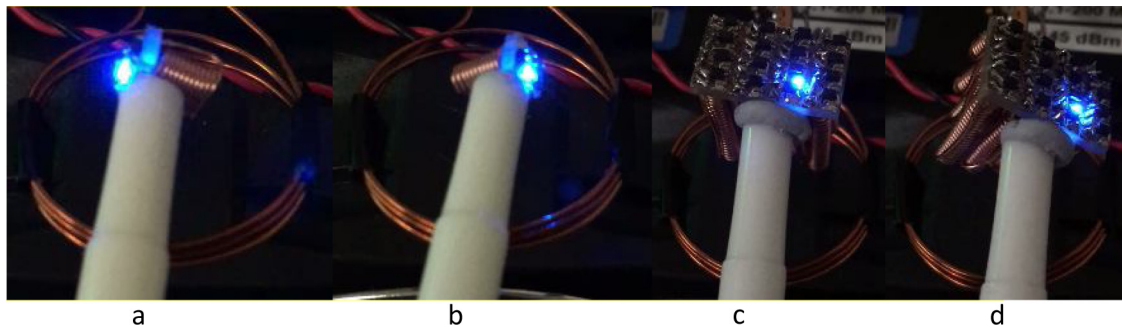


Fig. 9. Influence of misalignment on dual channel and 16 channel devices. Each pair of figures shows the angular range within which the selected channel remains activated.

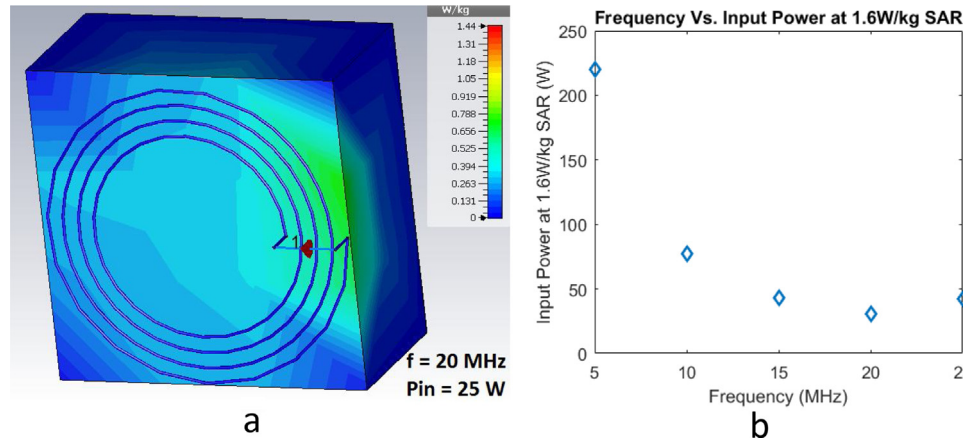


Fig. 10. a) Depiction of CAD model used for electromagnetic simulation of transmitting coil above a volume of muscle tissue. At an input power of 25 W at 20 MHz, the maximum 1g averaged SAR is 1.44 W/kg, which is still below the safety threshold of 1.6 W/kg. b) The continuous input power to the coil required to exceed the safety threshold for SAR (specific absorption rate) of 1.6 W/kg averaged over 1 g of tissue.

and a mW/mm^2 value can be calculated by dividing the light output power by 0.5 mm^2 . When one carrier frequency and hence, LED is selected, the other channel is measured to ensure it is off. This is to confirm that the channel selectivity is sufficiently significant to stop the 13.4 MHz signal driving the tank tuned to 15.6 MHz and vice versa. It was observed that at 10 W input power and at a transmission distance less than 3 mm, signal interference did occur resulting in both LEDs being activated.

3.4. Channel selectivity

The ability to address individual channels across two, dual channel devices is shown in Fig. 7. The devices are separated from the transmitting coil by 11 mm and the input power is set to 5 W. Each channel of each device is addressed by transmitting a sine wave of frequency 13.4 MHz, 15.6 MHz, 16.2 MHz and 17.8 MHz. The corresponding response of each transmitted frequency is pictured from left to right. The capacitor bank switches are adjusted to allow for optimum tuning. This is done by observing the LEDs to determine maximum brightness for a given switch configuration. The resonant frequency of each channel is spaced enough such that no channel interference is observed. Identical channel selectivity behaviour was observed with the devices embedded in porcine tissue.

The ability to address multiple channels simultaneously is shown in Fig. 8, with the 16 channel device. Channels 1–4 are numbered from top right to top left with channel 16 in the bottom left corner. The device is separated from the transmitter by 5.5 mm. Channel 6 is addressed by setting the transmitted power and frequency to 5 W and 15.4 MHz. This is depicted in Fig. 8a. A sinusoidal frequency sweep from 12 MHz to 20 MHz activates channels one to 12 in Fig. 8b and all channels are shown to be working with a sweep

from 12 MHz to 27 MHz in Fig. 8c. Due to tuning considerations and varying coil sizes, each light varies in brightness with the frequency sweep. However, this is solved using an arbitrary waveform that varies the transmitted power with frequency. Once again, identical channel selectivity behaviour was observed in porcine tissue.

3.5. Angular displacement

The influence of angular displacement on power transfer is depicted in Fig. 9. Fig. 9a and b show a test of a dual channel device. The device could be turned counter clockwise to 80° with the channel remaining activated. This was limited to 70° when turning the device clockwise. A similar test was performed for the 16 channel device as shown in Figs. 9c and d. The dual channel device demonstrates greater tolerance to angular displacement than the 16 channel device.

3.6. Tissue heating

Fig. 10 depicts how the transmitting coil heats tissue. Fig. 10a shows the CAD model used with the coil above a volume of muscle tissue. Fig. 10b shows that the safety limit of 1.6 W/kg is only reached when the transmitting power is much larger than 10 W, the maximum transmitting power used in this work. This is particularly evident for a transmitting frequency of 5 MHz, where over 200 W of input power is required to breach the safety threshold. Fig. 10b also assumes that the carrier frequency is continuously transmitting. This is known not to be the case, since modulation is a requirement of optogenetic systems as depicted in Fig. 11. Therefore, a more accurate input power threshold can be realised by multiplying the maximum input power by the reciprocal of the modulation duty

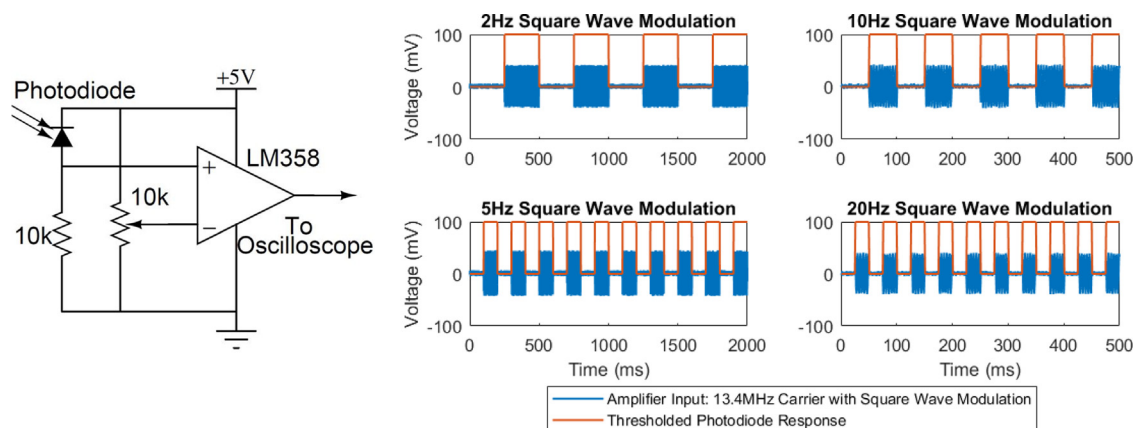


Fig. 11. Square wave modulation of carrier frequency superimposed onto the photodiode response to the light source for modulation frequencies of 2 Hz, 5 Hz, 10 Hz and 20 Hz. The voltage scale refers to the amplifier input signal, whereas the photodiode response is binary.

cycle. For example, in Fig. 11, the carrier frequency is on 50% of the time, meaning the duty cycle is 50%, meaning the maximum input power transmitted by the coil could be doubled before safety thresholds were reached.

3.7. Frequency response and in-vitro cell study

Light modulation is an essential requirement for optogenetic experiments and is shown in Fig. 11. The behaviour shown in Fig. 11 was observed for modulation frequencies of up to 1 kHz. Fig. 12 depicts the response of a RGC to a single channel device. The cell exhibited spontaneous activity when the device was switched off. When the device was modulated, the RGC responded precisely to the stimulus such that bursts of action potentials occurred in synchrony with the light stimulus. The activity of the RGC is clearly in synchrony with the modulated single channel device, indicating the cell is an ON type cell. Fig. 13 shows the response of HEK-293 cells to a dual channel device. The cells were held at -60 mV and illumination while blue light evoked a robust inward current. This is consistent with the opening of a light-sensitive, cation-conducting ion channel. The responses followed repetitive light stimulation at 1–10 Hz (Fig. 13). When the cells were held at positive potentials the current reversed to outward, consistent with the opening of a cationic channel. Stimulation with yellow light did not evoke a response. Removal of the electrode from the cell was also without effect.

4. Discussion

An optogenetic stimulator needs to provide spatiotemporal resolution, sufficient light intensity, multiple channels and modulation capability. This work demonstrates that spatial resolution can be achieved with individual channels spaced as close as 2.5 mm apart. Power outputs of up to 15 mW are shown, which converts to 30 mW/mm² based on the LED surface area. The light output power at 590 nm is limited compared to that at 473 nm, due to LED efficiency. Several reports describe varying light power density requirements ranging from below 1 mW/mm² to 10 mW/mm², being largely dependent on implant location and the light delivery method used [23–26]. Light pulsing requirements are also met by using modulation on the transmitted sinusoidal carrier wave. Square wave modulation at 2 Hz, 5 Hz, 10 Hz and 20 Hz was measured with a photodiode and was also shown to work up to 1 kHz. Modulation requirements do not typically exceed 50 Hz in the literature, meaning that the modulation strategy used in this work is more than sufficient. Testing of a single channel and dual channel device on RGC and HEK-293 cells, provides biological validation.

The magnetic field produced by the transmitter did not appear to adversely affect the cells. At 5 Hz and 10 Hz square wave modulation, the HEK-293 cells did not recover entirely. However, this could be changed by using pulsed modulation to increase recovery time or by increasing the light intensity [4], both of which are possible with the system described in this work. As expected, HEK-293 cells did not respond to yellow light, providing biological validation of the channel selectivity feature in Fig. 6. Addressing multiple channels simultaneously is achieved through multiplexing, but this presents a limitation. That is, less optical power is available for each individual channel as it is shared between channels. However, if this is taken into consideration at the design phase, sufficient light output power can be made available.

All measurements were done in air, as well as in porcine tissue for biological validation and results were found to differ by no more than 3% in the two media. This is surprising, as electromagnetic fields and waves are known to interact with tissue. Nevertheless, the result can be understood by appreciating the subtleties of the experimental setups described in this work. Wireless power transfer in this work is due to inductive coupling in the quasi-static magnetic near field of the transmitting coil. The relative magnetic permeability of biological tissue is close to unity [27]. Hence, a magnetic field sees biological tissue much like it sees air. However, this is not the case for the frequency dependent relative permittivity, which is around 100 for muscle in the frequency range used in this work [28]. Out of all biological media, muscle is used since it has average electrical characteristics. Due to the high relative permittivity of muscle, the extra parasitic capacitance created by the surrounding porcine tissue should influence the resonant frequency and quality factor measurements. Moreover, the lossy nature of the parasitic capacitance due to its conductivity should reduce light output power. Why then, does biological tissue have such a negligible effect on these variables in these experiments? There are three probable reasons: C_{RX} is large compared to the parasitic capacitance, the inside of each receiving coil L_{RX} does not contain porcine tissue and the receiving resonant tank is loaded with an LED.

The majority of solenoid self-capacitance emerges between windings, and on the inside of the coil. The capacitance emerging from the outside is much less, in this work likely less than a 1 pF based on the measurement results. Even when the coil is surrounded by biological material with relative permittivity of 100, the increase in parasitic capacitance is negligible compared to the choice of tuning capacitors that range from 910 pF to 1200 pF. This explains the limited influence of porcine tissue on f_{RES} and Q . The negligible influence of porcine tissue on light output power can be understood by appreciating that the LEDs place considerable load

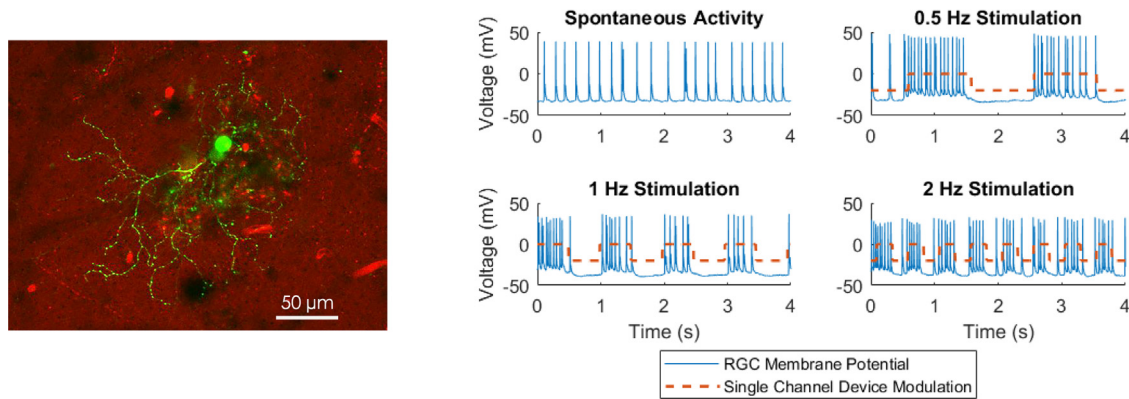


Fig. 12. Retinal ganglion cell morphology and response to light stimuli generated by a single channel device. Left) A confocal reconstruction of the retinal ganglion cell recorded and labelled with Alexa 488 (green) with the extracellular spaces labelled with Sulforhodamine 101 (red). Right) Recordings of the retinal ganglion cell in response to light stimulation (For interpretation of the references to color in this figure legend, the reader is referred to the web version of this article.).

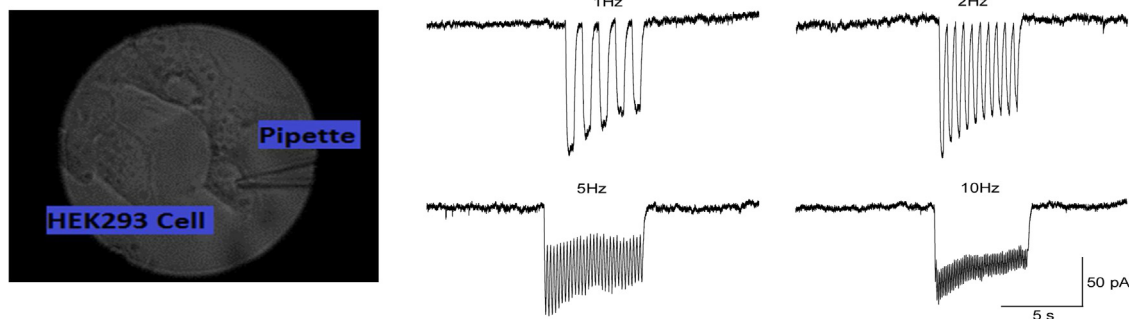


Fig. 13. HEK-293 cells were transfected with blue-sensitive opsin for 48 h (left) and studied under patch-clamp. The cells were held at -60 mV and stimulation with blue light evoked robust inward currents.

Table 4
State of the Art Review.

Reference	Number of channels	Wireless method	Input power	Device mass	Longest device dimension
This work	4	Inductive	Up to 10 W	1g	5 mm
This work	16	Inductive	Up to 10 W	6.5 g	20 mm
[7]	1	Radiative	4W	–	2 mm
[8]	Up to 3	Radiative	<1 W	33 mg	5 mm
[9]	1	Inductive	Up to 12 W	30 mg	10 m

on the resonant receiving tank, in the order of 100Ω . The loss due to the surrounding porcine tissue is easily an order of magnitude or two less than the power consumed by the load.

Angular displacement or coil misalignment has greater effect with an increase in the number of channels as depicted in Fig. 10. The dual channel device is slightly more tolerant to counter clockwise angular displacement. In Fig. 10a and b, the left coil is driving the blue LED, meaning the right coil attenuates the received signal. The same effect can be observed in Fig. 10c and d, and is more significant due to the increased number of coils blocking the signal.

In its current form the device still requires biocompatible packaging that permits transmission of light. For short term applications, low temperature melting glass or epoxy are likely to suffice as an encapsulate. For longer term implantation, a previously reported method of forming hermetic packages from diamond and gold braze could be suitable [29]. Moreover, receiving coils could be embedded into the diamond substrate itself [30]. It is known that diamond has high transmittance in visible wavelengths and causes negligible immune response making it potentially suitable for this application [31].

Eqs. (8) and (9) for calculating the inductance of a solenoid differ by an order of magnitude. However, they do bound the measured

inductances, which can be explained by the origins of each formula. Eq. (9) assumes that the wire used is an infinitely thin filament, which is not the case as the winding thickness is 20% of the coil diameter [32–33]. Eq. (8) on the other hand is empirical and was initially devised as an approximation of the inductance of a loop antenna [17]. As the number of turns increases, Eq. (8) over approximates inductance. Nevertheless, Eqs. (8) and (9) are useful bounds for approximation.

The different coil sizes mean the power transfer efficiency differs for each channel. This is shown by the scaling factor P_{OUT}/P_{MAX} in Table 3. A strategy that could be used to compensate for this difference is driving each channel with a different input power. Most signal generators can be programmed to deliver waveforms of arbitrary amplitude and frequency. This technique was used for channel selection by varying frequency and can be extended to include amplitude to provide a constant light output per channel.

Table 4 provides a comparison between this work and other miniature wireless optogenetic devices. Studies [7,8] demonstrate that their devices work in home cages, whereas this work focuses on the design equations used, bench top characterization and in-vitro cell studies. The wireless system in this work could be used in a home cage where the coils form part of the platform. Since

the transmitter coil is 30 mm in diameter, it would take several coils to cover a reasonable area, increasing power consumption, although, such a configuration would also reduce SAR dramatically. The size of the transmitting coil and mass of the devices in this work means it is likely more suited to a large animal model, where the animal can wear the coil above its skin, above the location of the implanted optogenetic device. There are several advantages to having a wireless link between a wearable coil and an implant. Infection is less likely to occur since percutaneous wires are not used [34–36] and transcutaneous wire breakages would not occur. Furthermore, from a design perspective, this work emphasizes that variables such as coil quality factor and power transfer efficiency can be traded for an increase in the number of individual channels. Hence, this work is useful for the optogenetic user, as the implant design is simple and uses only readily available components. The techniques described herein provides researchers involved in optogenetics with a tool kit for creating bespoke, multiple wavelength, implantable, individually tunable devices.

This work describes a multichannel inductively coupled link for the purposes of wireless optogenetic stimulation. By encoding light intensity, modulation and channel selection into the transmitted carrier wave, complex electronics are removed from the implant. Light output power, modulation and channel selection are all verified experimentally in various configurations and biological settings to demonstrate design efficacy. Moreover, readily available components are used for all aspects of the design, making the described technique accessible to researchers.

Author contributions

Unless otherwise stated, AA conceived, designed, fabricated and performed all experiments in this work and wrote the manuscript. WT dissected the retina, wrote paragraph 1 of Section 2.5 and created the cell figure in 12. ASB patched the retina and recorded data for Fig. 12. ASB, WT and AA conceived the experiment in Fig. 4. GC transfected and mounted the HEK293 cells and wrote paragraph 2 of Section 2.5. HAC, HCP, MAT and AA conceived the experiment in Fig. 13. MAT patched the HEK293 cells and HAC and HCP advised on the experiment. MAT and HCP created Fig. 12. JMR advised on the simulation in Fig. 10 and all authors were responsible for reviewing the manuscript and providing edits and feedback.

Declaration of interest

SP is a shareholder, director and chief technology officer of iBionics, a company developing a diamond based retinal implant.

Acknowledgements

The authors would like to thank Stephen Gregory for fabricating the printed circuit boards and Deisseroth lab for providing the plasmid. In addition to the anonymous reviewers the authors would also like to thank Jemma Wiseman for proof reading and providing additional comments and feedback. This work was funded by the National Health and Medical Research Council (NHMRC) of Australia, grant GNT1101717.

Appendix A. Supplementary data

Supplementary material related to this article can be found, in the online version, at doi: <https://doi.org/10.1016/j.sna.2017.12.051>

References

- [1] A.R. Adamantidis, F. Zhang, A.M. Aravanis, K. Deisseroth, L. de Lecea, Neural substrates of awakening probed with optogenetic control of hypocretin neurons, *Nature* 450 (2007) 420–424.
- [2] P.R. Albert, Light up your life: optogenetics for depression? *J. Psychiatry Neurosci.* 39 (2014) 3–5.
- [3] J.A. Steinbeck, S.J. Choi, A. Mrejeru, Y. Ganat, K. Deisseroth, D. Sulzer, et al., Optogenetics enables functional analysis of human embryonic stem cell-derived grafts in a Parkinson's disease model, *Nat. Biotechnol.* 33 (2015) 204–209.
- [4] E.S. Boyden, F. Zhang, E. Bamberg, G. Nagel, K. Deisseroth, Millisecond-timescale, genetically targeted optical control of neural activity, *Nat. Neurosci.* 8 (no. 9) (2005) 1263–1268.
- [5] M. Auffret, V.L. Ravano, G.M. Rossi, N. Hankov, M.F. Petersen, C.C. Petersen, Optogenetic stimulation of cortex to map evoked whisker movements in awake head-restrained mice, *Neuroscience* (2017).
- [6] C. Hung, G. Ling, S. Mohanty, J. Chiao, An integrated microLED optrode for optogenetic stimulation and electrical recording, *IEEE Trans. Biomed. Eng.* 60 (2013) 225.
- [7] K.L. Montgomery, A.J. Yeh, J.S. Ho, V. Tsao, S.M. Iyer, L. Grosenick, et al., Wirelessly powered, fully internal optogenetics for brain, spinal and peripheral circuits in mice, *Nat. Methods* 12 (2015) 969.
- [8] S.I. Park, G. Shin, J.G. McCall, R. Al-Hasani, A. Norris, L. Xia, et al., Stretchable multichannel antennas in soft wireless optoelectronic implants for optogenetics, *Proc. Natl. Acad. Sci. U. S. A.* 113 (2016) 8169.
- [9] G. Shin, A.M. Gomez, R. Al-Hasani, Y.R. Jeong, J. Kim, Z. Xie, et al., Flexible near-field wireless optoelectronics as subdermal implants for broad applications in optogenetics, *Neuron* 93 (2017) 509–521.
- [10] Y. Zhao, L. Tang, R. Rennaker, C. Hutchens, T.S. Ibrahim, Studies in RF power communication, SAR, and temperature elevation in wireless implantable neural interfaces, *PLoS One* 11 (2013) e77759.
- [11] H. Lee, K.Y. Kwon, W. Li, M. Ghovanloo, A power-efficient switched-capacitor stimulating system for electrical/optical deep brain stimulation, *IEEE J. Solid-State Circuits* 50 (2015) 360–374.
- [12] M. Schwaerzle, F. Pothof, O. Paul, P. Ruther, High-resolution neural depth probe with integrated 460 nm light emitting diode for optogenetic applications, 18th International Conference on Solid-State Sensors, Actuators & Microsystems 18 (2015) 1774–1777.
- [13] C.T. Wentz, J.G. Bernstein, P. Monahan, A. Guerra, A. Rodriguez, E.S. Boyden, A wirelessly powered and controlled device for optical neural control of freely-behaving animals, *J. Neural Eng.* 8 (2011) 046021.
- [14] Mark A. Rossi, Vinson Go, Tracy Murphy, Quanhai Fu, James Morizio, Henry H. Yin, A wirelessly controlled implantable LED system for deep brain optogenetic stimulation, *Front. Integr. Neurosci.* 9 (2015).
- [15] R.P. Kale, A.Z. Kouzani, K. Walder, M. Berk, S.J. Tye, Evolution of optogenetic microdevices, *Neurophotonics* 2 (2015) 031206.
- [16] R. Jegadeesan, G. Yong-Xin, Topology selection and efficiency improvement of inductive power links, *IEEE Trans. Antennas Propag.* (10) (2012), 4846.
- [17] R.C. Johnson, H. Jasik, *Antenna Engineering Handbook*, McGraw-Hill, New York, London, 1961.
- [18] H.-Y. Chen, H.-H. Wang, Current and SAR induced in a human head model by the electromagnetic fields irradiated from a cellular phone, *IEEE Trans. Microw. Theory Techn.* 42 (12) (1994) 2249–2254.
- [19] R.C. Wong, S.L. Cloherty, M.R. Ibbotson, B.J. O'Brien, Intrinsic physiological properties of rat retinal ganglion cells with a comparative analysis, *J. Neurophysiol.* 108 (no. 7) (2012) 2008–2023.
- [20] S.L. Cloherty, R.C. Wong, A.E. Hadjinicolaou, H. Meffin, M.R. Ibbotson, B.J. O'Brien, Epiretinal electrical stimulation and the inner limiting membrane in rat retina, *Eng. Med. Biol. Soc.* (2012).
- [21] O.P. Hamill, A. Marty, E. Neher, B. Sakmann, F.J. Sigworth, Improved Patch Clamp techniques for high Resolution current recording from cells and cell-free membrane patches, *Eur. J. Physiol.* 391 (1981) 85–100.
- [22] A. Hadjinicolaou, C. Savage, N. Apollo, D. Garrett, S. Cloherty, M. Ibbotson, B. O'Brien, Optimizing the electrical stimulation of retinal ganglion cells, *IEEE Trans. Neural Syst. Rehabil. Eng.* 2 (2014) 169.
- [23] I. Carcea, M.N. Insanally, R.C. Froemke, Dynamics of auditory cortical activity during behavioural engagement and auditory perception, *Nat. Commun.* 8 (2017) 14412.
- [24] Y. Song, J. Kim, H. Jeong, I. Choi, D. Jeong, K. Kim, S. Lee, A neural circuit for auditory dominance over visual perception, *Neuron* 93 (2017) 940–954.
- [25] J.M. Otis, V.K. Nambodiri, A.M. Matan, E.S. Voets, E.P. Mohorn, O. Kosyk, et al., Prefrontal cortex output circuits guide reward seeking through divergent cue encoding, *Nature* 543 (2017) 103.
- [26] C.D. Howard, H. Li, C.E. Geddes, X. Jin, Dynamic nigrostriatal dopamine biases action selection, *Neuron* 93 (2017) 1436–1450.
- [27] H. Scharfetter, R. Casanas, J. Rosell, Biological tissue characterization by magnetic induction spectroscopy (MIS): requirements and limitations, *IEEE Trans. Biomed. Eng.* 50 (7) (2003) 870–880.
- [28] S. Gabriel, R.W. Lau, C. Gabriel, The dielectric properties of biological tissues: II. measurements in the frequency range 10 Hz to 20 GHz, *Phys. Med. Biol.* 41 (11) (1996) 2251–2269.
- [29] S.G. Lichter, M.C. Escudé, A.D. Stacey, K. Ganesan, K. Fox, A. Ahnood, et al., Hermetic diamond capsules for biomedical implants enabled by gold active braze alloys, *Biomaterials* 53 (2015) 464–474.

- [30] M.U. Sikder, J. Fallon, M.N. Shivdasani, K. Ganesan, P. Seligman, D.J. Garrett, Wireless induction coils embedded in diamond for power transfer in medical implants, *Biomed. Microdevices* (4) (2017) 1.
- [31] D.J. Garrett, A.L. Saunders, C. McGowan, J. Specks, K. Ganesan, H. Meffin, et al., In vivo biocompatibility of boron doped and nitrogen included conductive-diamond for use in medical implants, *J. Biomed. Mater. Res. Part B Appl. Biomater.* 104 (1) (2016) 19.
- [32] F.W. Grover, *Inductance Calculations: Working Formulas and Tables*, D. Van Nostrand, New York, 1946.
- [33] E.B. Rosa, F.W. Grover, *Formulas and tables for the calculation of mutual and self inductance*, *J. Wash. Acad. Sci.* (1911).
- [34] T. Saxena, L. Karumbaiah, E.A. Gaupp, R. Patkar, K. Patil, M. Betancur, et al., The impact of chronic blood–brain barrier breach on intracortical electrode function, *Biomaterials* 34 (2013) 4703–4713.
- [35] L. Karumbaiah, T. Saxena, D. Carlson, K. Patil, R. Patkar, E.A. Gaupp, et al., Relationship between intracortical electrode design and chronic recording function, *Biomaterials* 34 (2013) 8061–8074.
- [36] B.M. Ilfeld, R.A. Gabriel, M.F. Saulino, J. Chae, P.H. Peckham, S.A. Grant, et al., Infection rates of electrical leads used for percutaneous neurostimulation of the peripheral nervous system, *Pain Pract.* 17 (6) (2017) 753–762.

Biographies

Ammar Aldaoud Ammar received his bachelor degree in electrical and computer systems engineering with first class honours from Monash University. He is currently a Ph.D candidate enrolled in the School of Physics at the University of Melbourne, as well as a visiting student in the Howard Florey Laboratory and the Royal Melbourne Hospital. His current work is focusing on the design of novel wireless technology for biomedical electronics. More generally, his interests include RF design, antenna optimisation, EMC/EMI/RFI techniques, data transmission and analog/mixed-signal electronics.

Artemio Soto-Breceda Artemio is currently studying a PhD in biomedical engineering at The University of Melbourne, Australia, working mainly at the National Vision Research Institute. He obtained his Masters in bioelectronics from Cinvestav IPN, Mexico (2013), and his Bachelor Degree in electrical engineering at Autonomus University of Aguascalientes (UAA), Mexico (2010). He has been awarded a research scholarship from NICTA (Data 61, CSIRO, Australia) in 2014, the CONACYT research scholarship (Mexico) in 2011 and 2014, and The Peace Scholarship (IDP, Australia and SEP, Mexico) in 2008. Artemio's research interest focuses in understanding the behaviour of retinal ganglion cells during electrical stimulation.

Wei Tong Wei Tong received her B.S. degree from University of Science and Technology of China in 2012, and the Ph.D. degree from the University of Melbourne in 2017, both in Physics. She is currently a postdoc research fellow working at both National Vision Research Institute of Australia and the University of Melbourne. Her primary research focus is on designing neural interfaces with carbon based materials. She is now working on the optimisation of neural stimulation for the development of the IBIONICS diamond eye, a diamond-based high acuity retinal prosthesis.

Mary Tonta Mary has been a Research Assistant to Parking for 25 years and is highly trained in electrophysiological techniques.

Harold Coleman Harold obtained an Honours degree in Physics, followed by a PhD in Physiology, at Monash University in Melbourne. He is currently a Research Fellow in Physiology at Monash University and an Honorary Senior Research Fellow at the Florey Institute of Neuroscience and Mental Health. His research interests include using electrophysiological and imaging techniques to study the contribution of ion channels to the function and dysfunction of excitable cells in health and disease.

Helena Parkington The emphasis of Prof. Parkington's research is on function in excitable cells in health and disease. Her approach is one of "vertical integration" that encompasses ion channels in isolated cells, tissue reactivity and whole animal studies in rodents, sheep and humans. The critical role of ion channels in the functioning of excitable cells means that electrophysiology is a core expertise.

Iain Clarke Professor Clarke graduated from Massey University, New Zealand (B. Agric. Sci., 1971) followed by M. Agric. Sci. (1st Class) in reproductive physiology in 1973). He then obtained his PhD at Edinburgh University, Scotland in 1976, studying endocrinology and behaviour. He then moved to Australia and has been in Melbourne since 1977. He became a Senior Research Fellow of NHMRC in 1986, rising to Senior Principal Research Fellow in 1998. He was Chairman, Department of Physiology, Monash University 2007–2016 and is now a Research Professor in the Department.

Jean-Michel Redoute Jean-Michel is a senior lecturer in analog electronics at Monash University. In September 2009, he started working at the Berkeley Wireless Research Center at the University of California, at Berkeley, for the length of one year as a postdoctoral scholar: this research was funded by the Belgian American Educational Foundation (BAEF). In September 2010, he joined Monash University as a senior lecturer. His research is concentrated on robust mixed-signal integrated circuit (IC) design with a high immunity to electromagnetic interference (EMI), electromagnetic compatibility (EMC), biomedical (integrated and non-integrated) circuit design and radio frequency integrated circuit design.

David Garrett David is a post-doctoral research fellow at the University of Melbourne, School of Physics. His interests include medical device development and carbon materials for neuromodulation. David's research efforts are targeted towards retinal prosthesis for the blind, as well as cortical to protect from epileptic seizure.

Steven Prawer Steven Prawer has a worldwide reputation in advanced diamond science and technology with over 25 years of experience and over 250 scientific publications. Professor Prawer is currently a senior leader one of Australia's most prestigious national projects dedicated to the development of a bionic eye. He leads the team to develop the high density electrode array plus encapsulation strategy capable of delivering a high acuity device which will enable profoundly blind people to once again be able to recognize the faces of loved ones and read large print.